
RESTRICTED BOLTZMANN MACHINE REPRESENTATION FOR THE GROUNDSTATE AND EXCITED STATES OF KITAEV HONEYCOMB MODEL

A PREPRINT

Mohammadreza Noormandipour^{*,a}, Youran Sun^{†,b}, Babak Haghighat^{‡,b}
^a *DAMTP, University of Cambridge, Wilberforce Road, Cambridge CB3 0WA, UK*
^b *Yau Mathematical Sciences Center, Tsinghua University, Beijing, 100084, China*

March 9, 2020

ABSTRACT

In this work, the capability of restricted Boltzmann machines (RBMs) to find solutions for the Kitaev honeycomb model is investigated. The measured groundstate (GS) energy of the system is compared and shown to reside within less than 5% error of the analytically derived value of the energy. Furthermore, the possibility of realizing anyons in the RBM is discussed and an algorithm is given to build these anyonic excitations and braid them as a proof of concept for performing quantum gates and doing quantum computation. Moreover, the phase transition of the system is also studied by changing the corresponding hyper-parameters of the system in the RBM solution.

Keywords Restricted Boltzmann Machine (RBM) · Feed-Forward Neural Network (FFNN) · Honeycomb Lattice Model · Quantum State Tomography (QST) · Topological Phases of Matter · Anyons · Quantum Computing

1 Introduction

The Honeycomb model is a 2-dimensional lattice spin system (see Fig.1) which was first introduced by Kitaev in 2006 [1] and is famous because of the topological quantum order due to a degenerate gapped groundstate which is persistent to local and finite-sized perturbations. The system also supports both abelian and non-abelian topological phases as demonstrated in the original proposal [1]. There is a wide range of applications for this model, from fault-tolerant quantum computation [2] to analytical study of strongly correlated systems [3] and quantum spin liquids [4]. The honeycomb lattice is not a Bravais lattice in its original structure, but it can be considered as a triangular Bravais lattice with a two-spin basis. The direct Bravais lattice and the primitive cells are illustrated in Fig.1a with the dashed lines. Each primitive cell has a pair of odd and even indexed spins. Just for the sake of simplicity we will denote each cell with the even indexed (empty circles) spins of the system. The primitive vectors of the lattice, \mathbf{a}_1 and \mathbf{a}_2 are also shown in Fig.1a (see also Equ.1). The entire lattice can be tiled and covered with primitive cells using translations composed of different linear combinations of primitive vectors.

$$\mathbf{a}_1 = \sqrt{3}a\mathbf{e}_x \quad \& \quad \mathbf{a}_2 = \frac{\sqrt{3}}{2}a(\mathbf{e}_x, \sqrt{3}\mathbf{e}_y) \quad (1)$$

Where a is the lattice constant. The reciprocal lattice for the triangle lattice can be obtained by solving Equ.2 for basis vectors of the reciprocal lattice, \mathbf{b}_1 and \mathbf{b}_2 .

$$\mathbf{a}_i \cdot \mathbf{b}_j = 2\pi\delta_{ij} \quad (2)$$

^{*}mrn31@cam.ac.uk

[†]syouran0508@gmail.com

[‡]babakhaghighat@tsinghua.edu.cn

The solution is as below:

$$\mathbf{b}_1 = \frac{2\pi}{\sqrt{3}a}(\mathbf{e}_x - \frac{1}{\sqrt{3}}\mathbf{e}_y) \quad \& \quad \mathbf{b}_2 = \frac{4\pi}{3a}\mathbf{e}_y \quad (3)$$

The reciprocal lattice is depicted in Fig. 1b.

The Hamiltonian of the Kitaev model is a nearest-neighbor interaction of Pauli matrices on a honeycomb lattice as written in Equ.4, where r & r' are indices for the nearest neighbour spins. The physics of the system is symmetric under permutation of coupling strengths J_α with $\alpha = x, y, z$ and due to an-isotropic interaction the model is a frustrated spin system, because a spin cannot satisfy conflicting demands of orientation from its three neighboring sites [1].

$$H = - \sum_{\alpha} J_{\alpha} \sum_{\alpha-bonds} \sigma_r^{\alpha} \sigma_{r'}^{\alpha} \quad (4)$$

In this paper we apply the approach developed in [5] to the Honeycomb model. In Section2, we briefly review the analytical solution of the model. In Section3 the mapping of the spin model to an RBM architecture is explained. In particular, we demonstrate how to calculate the groundstate and excited states of the Honeycomb model using machine learning techniques. To this end we employ the NetKet environment [6] to train a restricted Boltzmann machine (RBM) in order to find a groundstate via gradient decent. In Section4 realization of vortices is discussed from both analytical and RBM language points of view. In brief, a vortex pair can be created by adjusting the parameters of the RBM and subsequent braiding can be achieved by further adjustments of parameters. Section5 is dedicated to results and relevant discussions and finally we conclude in Section6. An important application of the techniques developed in this paper is the reconstruction of a given quantum state from simple measurements known as quantum state tomography [7].

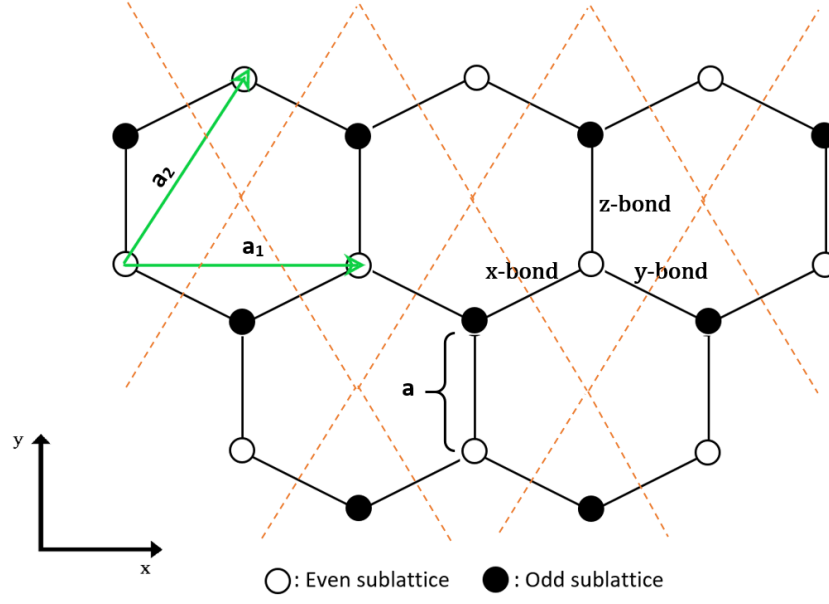
2 Solution of the Model

In this section an exact solution of the system is provided and an explicit form of the groundstate energy is achieved. First of all, we fermionize the Hamiltonian by performing a one-dimensional Jordan-Wigner transformation [8] defined in Equ.5. A deformation of the hexagonal lattice to a brick-wall lattice (see Fig.2) clarifies the mechanism of the Jordan-Wigner transformation and why it is one-dimensional [9]. In the brick-wall lattice, each lattice site r is denoted by the coordinates (i, j) .

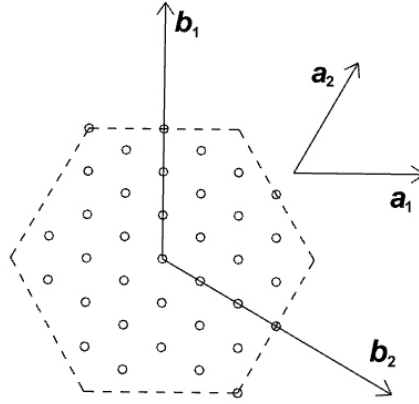
$$\begin{aligned} \sigma_{i,j}^+ &= 2[\prod_{j' < j} \prod_{i'} \sigma_{i',j'}^z][\prod_{i' < i} \sigma_{i',j}^z] a_{i,j}^\dagger \\ \sigma_{i,j}^- &= 2[\prod_{j' < j} \prod_{i'} \sigma_{i',j'}^z][\prod_{i' < i} \sigma_{i',j}^z] a_{i,j} \\ \sigma_{i,j}^z &= 2a_{i,j}^\dagger a_{i,j} - 1 \end{aligned} \quad (5)$$

This transformation maps the Hilbert space of spins to the Hilbert space of spinless complex fermions. Using the fact that $\sigma^\pm = \sigma^x \pm i\sigma^y$ one can expand the Hamiltonian in Equ.4 into three terms and rewrite them as below [10].

$$\begin{aligned} \sigma_{i,j}^x \sigma_{i+1,j}^x &= \prod_{i' < i} \sigma_{i',j}^z (a_{i,j}^\dagger + a_{i,j}) \prod_{i' < i+1} \sigma_{i',j}^z (a_{i+1,j}^\dagger + a_{i+1,j}) \\ &= (a_{i,j}^\dagger + a_{i,j}) \sigma_{i,j}^z (a_{i+1,j}^\dagger + a_{i+1,j}) \\ &= -(a_{i,j}^\dagger - a_{i,j}) (a_{i+1,j}^\dagger + a_{i+1,j}) \\ \sigma_{i,j}^y \sigma_{i+1,j}^y &= - \prod_{i' < i-1} \sigma_{i',j}^z (a_{i-1,j}^\dagger - a_{i-1,j}) \prod_{i' < i} \sigma_{i',j}^z (a_{i,j}^\dagger - a_{i,j}) \\ &= -(a_{i-1,j}^\dagger - a_{i-1,j}) \sigma_{i-1,j}^z (a_{i,j}^\dagger - a_{i,j}) \\ &= (a_{i-1,j}^\dagger + a_{i-1,j}) (a_{i,j}^\dagger - a_{i,j}) \\ \sigma_{i,j}^z \sigma_{i,j+1}^z &= (2a_{i,j}^\dagger a_{i,j} - 1) (2a_{i,j+1}^\dagger a_{i,j+1} - 1) \end{aligned} \quad (6)$$



(a)



(b)

Figure 1: (a) The honeycomb lattice in position space and its primitive vectors and primitive cell. (b) First Brillouin zone and primitive vectors of reciprocal lattice.

Therefore, the Hamiltonian transforms to the one in Equ.7.

$$\begin{aligned}
 H = & + J_x \sum_{x-links} (a_{i,j}^\dagger - a_{i,j})(a_{i+1,j}^\dagger + a_{i+1,j}) \\
 & - J_y \sum_{y-links} (a_{i-1,j}^\dagger + a_{i-1,j})(a_{i,j}^\dagger - a_{i,j}) \\
 & - J_z \sum_{z-links} (2a_{i,j}^\dagger a_{i,j} - 1)(2a_{i,j+1}^\dagger a_{i,j+1} - 1)
 \end{aligned} \tag{7}$$



Figure 2: Brick-wall lattice and the Jordan-Wigner transformation path depicted with the dashed arrows. The \mathbf{r}_1 and \mathbf{r}_2 are the primitive vectors for this lattice.



Figure 3: Kitaev Honeycomb lattice model on a torus: The generators of the lattice in position space are named \mathbf{e}_1 and \mathbf{e}_2 , as shown in the image above. Hence, the lattice points are $\mathbf{L} = n_1\mathbf{e}_1 + n_2\mathbf{e}_2$ with $n_1, n_2 \in \mathbb{Z}$ and the above lattice is drawn for $N_1 = N_2 = 4$ with toric boundary conditions.

The J_x and J_y terms are quadratic interactions in spinless fermions and are easy to solve, however, the J_z term is a product of number density operators and can be further simplified by introducing the Majorana operators in Equ.8 [10]. As we will see, this simplification can be done due to the presence of the conserved quantity called plaquette operator B_p [10].

$$\begin{aligned} c_{i,j} &= i(a_{i,j}^\dagger - a_{i,j}) \quad , \quad d_{i,j} = a_{i,j}^\dagger + a_{i,j} \quad , \quad \text{for } i+j = \text{even} \equiv \circ \\ c_{i,j} &= a_{i,j}^\dagger + a_{i,j} \quad , \quad d_{i,j} = i(a_{i,j}^\dagger - a_{i,j}) \quad , \quad \text{for } i+j = \text{odd} \equiv \bullet \end{aligned} \quad (8)$$

These operators have the following commutation relations:

$$\begin{aligned} c_{i,j}^2 &= d_{i,j}^2 = 1 \\ \{c_{i,j}, c_{i',j'}\} &= \{d_{i,j}, d_{i',j'}\} = 2\delta_{ii'}\delta_{jj'} \\ \{c_{i,j}, d_{i',j'}\} &= 0 \end{aligned} \quad (9)$$

Then, the J_z term can be rewritten using the Majorana operators:

$$\begin{aligned} \sigma_{i,j}^z \sigma_{i,j+1}^z &= (2a_{i,j}^\dagger a_{i,j} - 1)(2a_{i,j+1}^\dagger a_{i,j+1} - 1) \\ &= i(id_{i,j+1} d_{i,j}) c_{i,j+1} c_{i,j} \end{aligned} \quad (10)$$

Finally, using the circle indices for the odd and even lattice sites as defined in Equ.8 the Hamiltonian transforms to the expression in Equ.11.

$$\begin{aligned} H &= -iJ_x \sum_{x\text{-links}} c_\circ c_\bullet \\ &\quad + iJ_y \sum_{y\text{-links}} c_\bullet c_\circ \\ &\quad - iJ_z \sum_{z\text{-links}} (id_\bullet d_\circ) c_\bullet c_\circ \end{aligned} \quad (11)$$

If we write the Hamiltonian as a sum over unit cells we have:

$$H = i \sum_{\mathbf{r}} [J_x c_{\bullet, \mathbf{r}} c_{\circ, \mathbf{r}+\mathbf{r}_1} + J_y c_{\bullet, \mathbf{r}} c_{\circ, \mathbf{r}+\mathbf{r}_2} - J_z (id_{\bullet, \mathbf{r}} d_{\circ, \mathbf{r}}) c_{\bullet, \mathbf{r}} c_{\circ, \mathbf{r}}] \quad (12)$$

where \mathbf{r} is the position vector of z-bonds or unit cells (see Fig.2). It makes no difference in the physics if we set \mathbf{r} to be any point along the z-bond, whether we choose an even site or an odd site or some point in the middle, they are all related through translation. What will be important in what follows, is that now since we have grouped a pair of even and odd sites as an unit cell, to evaluate the summation over the unit cells, it is sufficient to just run over the even or odd sites.

Furthermore, the $\alpha_{\mathbf{r}} = (id_{\bullet, \mathbf{r}} d_{\circ, \mathbf{r}})$ operators are defined on each z-bond of the lattice (labeled by \mathbf{r}) and they commute with the Hamiltonian and are good quantum numbers. Moreover, it can easily be shown that each plaquette operator can be written as:

$$B_p = \sigma_1^y \sigma_2^z \sigma_3^x \sigma_4^y \sigma_5^z \sigma_6^x = \alpha_{61} \alpha_{43} \quad (13)$$

On the other hand, from Lieb's theorem [11] we know that the groundstate manifold is obtained by setting $B_p = 1, \forall p$. Thus the uniform choice of $\alpha_{\mathbf{r}} = 1, \forall \mathbf{r}$ corresponds to a vortex-free sector, nevertheless all configurations leading to the same sector are equivalent.

We also introduce a Dirac fermion on each z-link using the Majorana operators:

$$\begin{aligned} d_{\mathbf{r}} &= \frac{1}{2}(c_{\bullet, \mathbf{r}} - ic_{\circ, \mathbf{r}}) \\ d_{\mathbf{r}}^{\dagger} &= \frac{1}{2}(c_{\bullet, \mathbf{r}} + ic_{\circ, \mathbf{r}}) \end{aligned} \quad (14)$$

Using the inverse transformation we can rewrite the Hamiltonian:

$$\begin{aligned} H &= \sum_{\mathbf{r}} [J_x(d_{\mathbf{r}}^{\dagger} + d_{\mathbf{r}})(d_{\mathbf{r}+\mathbf{r}_1}^{\dagger} - d_{\mathbf{r}+\mathbf{r}_1}) \\ &\quad + J_y(d_{\mathbf{r}}^{\dagger} + d_{\mathbf{r}})(d_{\mathbf{r}+\mathbf{r}_2}^{\dagger} - d_{\mathbf{r}+\mathbf{r}_2}) \\ &\quad + J_z\alpha_{\mathbf{r}}(2d_{\mathbf{r}}^{\dagger}d_{\mathbf{r}} - 1)] \end{aligned} \quad (15)$$

The Hamiltonian is translation invariant and can be transformed to momentum space in order to be diagonalized. We define the Fourier transform for the Dirac fermion through:

$$\begin{aligned} d_{\mathbf{r}} &= \frac{1}{\sqrt{N}} \sum_{\mathbf{k}} e^{+i\mathbf{k} \cdot \mathbf{r}} d_{\mathbf{k}} \\ d_{\mathbf{r}}^{\dagger} &= \frac{1}{\sqrt{N}} \sum_{\mathbf{k}} e^{-i\mathbf{k} \cdot \mathbf{r}} d_{\mathbf{k}}^{\dagger} \end{aligned} \quad (16)$$

Setting $\mathbf{k} \rightarrow -\mathbf{k}$ in $d_{\mathbf{r}}^{\dagger}$ simplifies the calculations. We then have:

$$\begin{aligned} \mathbf{X} : & J_x \frac{1}{N} \sum_{\mathbf{r}} \sum_{\mathbf{k}, \mathbf{k}'} e^{+i\mathbf{k} \cdot \mathbf{r}} e^{+i\mathbf{k}' \cdot (\mathbf{r}+\mathbf{r}_1)} (d_{-\mathbf{k}}^{\dagger} + d_{\mathbf{k}})(d_{-\mathbf{k}'}^{\dagger} - d_{\mathbf{k}'}) \\ &= J_x \sum_{\mathbf{k}} [-2 \cos(k_1) d_{\mathbf{k}}^{\dagger} d_{\mathbf{k}} + i \sin(k_1) (d_{\mathbf{k}}^{\dagger} d_{-\mathbf{k}} - h.c.)] \\ \mathbf{Y} : & J_y \frac{1}{N} \sum_{\mathbf{r}} \sum_{\mathbf{k}, \mathbf{k}'} e^{+i\mathbf{k} \cdot \mathbf{r}} e^{+i\mathbf{k}' \cdot (\mathbf{r}+\mathbf{r}_2)} (d_{-\mathbf{k}}^{\dagger} + d_{\mathbf{k}})(d_{-\mathbf{k}'}^{\dagger} - d_{\mathbf{k}'}) \\ &= J_y \sum_{\mathbf{k}} [-2 \cos(k_2) d_{\mathbf{k}}^{\dagger} d_{\mathbf{k}} + i \sin(k_2) (d_{\mathbf{k}}^{\dagger} d_{-\mathbf{k}} - h.c.)] \\ \mathbf{Z} : & J_z \frac{1}{N} \sum_{\mathbf{r}} \sum_{\mathbf{k}, \mathbf{k}'} e^{+i\mathbf{k} \cdot \mathbf{r}} e^{+i\mathbf{k}' \cdot \mathbf{r}} (2d_{-\mathbf{k}}^{\dagger} d_{\mathbf{k}'}^{\dagger} - 1) \\ &= J_z \sum_{\mathbf{k}} 2d_{\mathbf{k}}^{\dagger} d_{\mathbf{k}} - J_z N. \end{aligned} \quad (17)$$

For the above equation we used the orthogonality relation in Fourier transformation:

$$\sum_{\mathbf{r}} e^{i(\mathbf{k}+\mathbf{k}') \cdot \mathbf{r}} = N\delta(\mathbf{k} + \mathbf{k}') \quad (18)$$

Using all previous transformations we obtain a Hamiltonian which is quadratic in the Dirac fermions living on each of the unit cells along the z-links:

$$\begin{aligned}
 H &= \sum_{\mathbf{k}} [\epsilon_{\mathbf{k}} d_{\mathbf{k}}^{\dagger} d_{\mathbf{k}} + \frac{1}{2} (i \Delta_{\mathbf{k}} d_{\mathbf{k}}^{\dagger} d_{-\mathbf{k}}^{\dagger} - i \Delta_{\mathbf{k}} d_{-\mathbf{k}} d_{\mathbf{k}})] - J_z N \\
 \epsilon_{\mathbf{k}} &= 2[J_z - J_x \cos(k_1) - J_y \cos(k_2)] \\
 \Delta_{\mathbf{k}} &= 2[J_x \sin(k_1) + J_y \sin(k_2)]
 \end{aligned} \tag{19}$$

By applying a unitary Bogoliubov transformation, we diagonalize the Hamiltonian which can be written as:

$$\begin{aligned}
 H &= \sum_{\mathbf{k}} \frac{1}{2} \begin{pmatrix} \gamma_{\mathbf{k}}^{\dagger} & \gamma_{-\mathbf{k}} \end{pmatrix} \begin{pmatrix} E_{\mathbf{k}} & 0 \\ 0 & -E_{\mathbf{k}} \end{pmatrix} \begin{pmatrix} \gamma_{\mathbf{k}} \\ \gamma_{-\mathbf{k}}^{\dagger} \end{pmatrix} \\
 &= \sum_{\mathbf{k}} E_{\mathbf{k}} \left(\gamma_{\mathbf{k}}^{\dagger} \gamma_{\mathbf{k}} - \frac{1}{2} \right), \quad E_{\mathbf{k}} = \sqrt{\epsilon_{\mathbf{k}}^2 + \Delta_{\mathbf{k}}^2},
 \end{aligned} \tag{20}$$

where $\gamma_{\mathbf{k}}^{\dagger}$ and $\gamma_{\mathbf{k}}$ are quasiparticle creation and annihilation operators. The groundstate energy can easily be read off from the above Hamiltonian and is given by $E_{GS} = -\sum_{\mathbf{k}} \frac{E_{\mathbf{k}}}{2}$.

3 Restricted Boltzmann Machine Representations

3.1 RBM as a Neural Network Quantum State

With the ever growing applications of neural networks in sciences and the emergent new technologies to deploy and build physical neural networks, this is the right time to investigate potential applications of them in condensed matter systems. Recently, a new approach has been proposed for simulating topological quantum states using neural networks [5]. In this section we use the same approach to map the Honeycomb Kitaev model to a restricted Boltzmann machine (RBM). There are many reasons why an RBM is chosen. This particular architecture has proved to be effective in many tasks such as dimensional reduction, classification, regression, collaborative filtering, feature learning and topic modeling and moreover a general theorem shows that RBMs are universal approximators of discrete distributions [12].

Having a set of spins on a lattice, $\Xi = (\sigma_1, \sigma_2, \dots, \sigma_N)$ (in our case the Jordan-Wigner chain of spins), our goal is to use an RBM to reduce the dimensionality of the Hilbert space and estimate the energy of the system in both groundstate and excited states to be able to classify different topological phases of the model. An RBM is a short range feed-forward neural network with two layers. The first layer (visible layer) has N nodes which are representing the physical spins in the Hamiltonian and the second layer (hidden layer) has M binary valued nodes (architecture of the network is shown in Fig.4).

The quantum state of the Honeycomb model, up to an irrelevant normalization factor, can be written as

$$|\Phi\rangle = \sum_{\Xi} \Phi_M(\Xi; \Omega) |\Xi\rangle \tag{21}$$

where

$$\begin{aligned}
 \Phi_M(\Xi; \Omega) &= \sum_{\{h_k\}} e^{\sum_k a_k \sigma_k^z + \sum_{k'} b_{k'} h_{k'} + \sum_{kk'} W_{kk'} h_k \sigma_k^z} \\
 &= e^{\sum_k a_k \sigma_k^z} \times \prod_{k'} \cosh \left(\sum_k W_{kk'} \sigma_k^z + b_{k'} \right)
 \end{aligned} \tag{22}$$

To obtain the second equality we used the values for $\{h_k\} = \{-1, 1\}^M$ which is the set of possible configurations of hidden layer nodes and $\Omega = (a_k, b_{k'}, W_{kk'})$ is the set of weights and biases of the RBM which should be trained in such

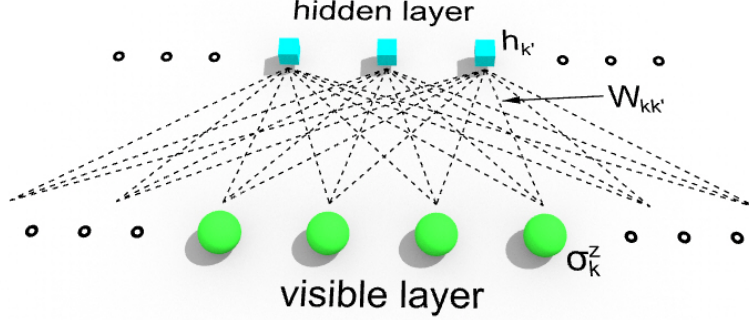


Figure 4: Fully connected Restricted Boltzmann machine architecture.

a way that the final RBM state represents the desired quantum state of the model (i.e. groundstate or the excited states). The combined number of weight and bias parameters and nodes is polynomial in system size and computationally feasible.

The mapping of the model to an RBM is done using the machinery already developed in the NetKet software package [6]. In order to train the network, the parameter space of the network was sampled using the Metropolis algorithm and the optimization iterations are based on the stochastic gradient descent algorithm.

3.2 Quantum State Tomography

Reconstruction of complex synthetic quantum states from experimental measurement data is computationally exponentially expensive. Therefore, the capability of neural network quantum states such as RBM to accurately and efficiently represent high-dimensional quantum states is beneficial to quantum state tomography. Apart from the numerous applications of QST, in our study case, the reconstructed states of the honeycomb model can later on be used for validation of particular quantum processes, e.g. braiding of vortices in the system, phase transitions, etc. at the experimental level and after implementation of the framework developed in Section 4. For instance, there are promising proposals for implementation of topological systems in cold atoms. A review has recently been published here [?].

In Section 5.3 we present QST results for the groundstate of a small system size of the honeycomb model, as proof of concept. In a normal QST task, the data sets come from experimental measurements, but since we don't have experimental data, we need to first find the exact wave-function for the system through exact diagonalization methods and then sample that wave-function by performing single shot measurements in different bases to build the data set.

After preparing the training data set, one needs to define a variational ansatz that should be trained on the measurement data. For the same motivations, we also choose an ansatz similar to the one used in [7]

$$\tilde{\psi}_{\lambda/\mu}(\sigma) = p_{\lambda}(\sigma) e^{i\phi_{\mu}(\sigma)} \quad (23)$$

where $\phi_{\mu}(\sigma) = \log p_{\mu}(\sigma)$ and $p_{\lambda/\mu}$ are RBM real probability distributions corresponding to two separate sets of RBM parameters λ/μ . The probability distribution of single shot measurements in basis b is given by

$$P_b(\sigma) = |\langle \sigma | \hat{U}_b | \Psi_U \rangle|^2 \quad (24)$$

where $|\Psi_U\rangle$ is the physical wave-function that we want to reconstruct. \hat{U}_b is the unitary transformation which rotates the wave-function to the basis b in which the measurement is performed. One can write the same expression for the probability distribution of the measurements for the variational wave-function $|\tilde{\psi}_{\lambda/\mu}\rangle$, namely $\tilde{P}_b(\sigma)$.

Then the QST problem reduces to a minimization task to find the set of parameters κ which minimizes the total Kullback-Leibler divergence between $P_b(\sigma)$ and $\tilde{P}_b(\sigma)$

$$\Xi(\kappa) = \sum_b \mathbb{KL}_b(\kappa) \quad (25)$$

where

$$\mathbb{KL}_b(\kappa) = \sum_{\sigma} P_b(\sigma) \log \frac{P_b(\sigma)}{\tilde{P}_b(\sigma)} \quad (26)$$

A more detailed explanation of how to perform this minimization using gradient descent can be found in [7]. The entire process of QST was implemented using NetKet [6] which has the above algorithm already built in.

4 Braiding

In this section we want to explore the possibility to create anionic excitations in the RBM representation and describe anyon braiding. Such a representation is important for various reasons, in particular for performing quantum computation [13].

First of all, let us describe the creation of these quasi-particles by starting with a groundstate sector and then subsequently changing the eigenvalue of the B_p operators from +1 to -1 locally and in the region where we want to realize the vortices in the system. In an arbitrary configuration of spins (not necessarily in the groundstate sector) it is easy to prove that $\prod B_p = +1, \forall p$. Hence, we can just build the vortices in pairs. For example, if you apply the operator \hat{O}_1 to the groundstate, it produces two vortices in plaquettes 1 and 2 (see Fig.5) [14] .

$$\hat{O}_1 = \exp \left(-i \frac{\pi}{2} \hat{\sigma}_a^z \right) \quad (27)$$

Another possibility is to apply the following operator

$$\hat{O}_2 = \exp \left(-i \frac{\pi}{2} \hat{\sigma}_a^x \right) \exp \left(-i \frac{\pi}{2} \hat{\sigma}_b^y \right), \quad (28)$$

which produces two vortices along the \hat{z} direction in plaquettes 3 and 4.

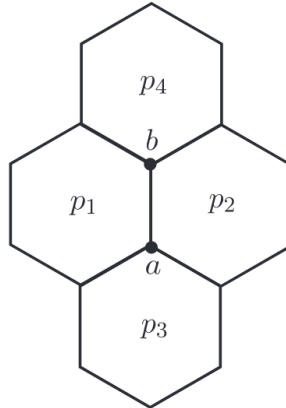


Figure 5: Caption

The reason why these operators can produce vortices in the system can be explained by rewriting the Hamiltonian of the system in terms of Majorana fermions. Kitaev originally solved the Hamiltonian through this approach. The disadvantage of this approach in comparison to what was done above is that when the Hamiltonian is mapped to Majorana fermions, there are unphysical states in the system which need to be projected out. This will be clear as we go along.

We assume that there are two fermionic modes living on each lattice site corresponding to the four creation and annihilation operators $a_{m,i}^\dagger$ and $a_{m,i}$, where $m \in \{1, 2\}$ is the index for the modes and i is the index for the lattice sites. Here unlike before, we use one index for lattice site to avoid unnecessary complications. Then we will separate the imaginary and real parts of these operators, to define the Majorana fermions as below

$$\begin{aligned} c_i &= a_{1,i} + a_{1,i}^\dagger \\ b_i^x &= i(a_{1,i}^\dagger - a_{1,i}) \\ b_i^y &= a_{2,i} + a_{2,i}^\dagger \\ b_i^z &= i(a_{2,i}^\dagger - a_{2,i}) \end{aligned} \quad (29)$$

Notice that the spins have a two dimensional space (being up or down) and now that we are representing them with four Majorana modes (two complex fermionic modes), we need to project out the unphysical states. The Fock space of the complex fermionic modes can be represented as $\{|00\rangle, |01\rangle, |10\rangle, |11\rangle\}$. We make the following correspondence between the states of spins and fermions

$$\begin{aligned} |\uparrow\rangle &= |00\rangle \\ |\downarrow\rangle &= |11\rangle \end{aligned} \quad (30)$$

We can define the projector P_i on site i to do this job for us

$$P_i = \frac{1 + D_i}{2} \quad \text{where} \quad D_i = (1 - 2a_{1,i}^\dagger a_{1,i})(1 - 2a_{2,i}^\dagger a_{2,i}) = b_i^x b_i^y b_i^z c_i. \quad (31)$$

One can easily show that the relation between Majorana operators and the original Pauli operators is as follows

$$\sigma_i^\alpha = i b_i^\alpha c_i \quad \text{for} \quad \alpha \in \{x, y, z\}. \quad (32)$$

In fact, by the above projection, we satisfied the extra condition coming from the algebra of Pauli matrices, $-i\sigma_i^x \sigma_i^y \sigma_i^z = b_i^x b_i^y b_i^z c_i = \mathbb{1}$. Therefore, the eigenvalue of the projector P_i for physical states is 1 and for unphysical states is 0.

Using Equ.32 the Hamiltonian can be written in terms of Majorana operators as

$$H = \frac{i}{2} \sum_{i,j} A_{ij} c_i c_j \quad \text{where} \quad A_{ij} = J_{ij} u_{ij} \quad \text{and} \quad u_{ij} = i b_i^\alpha b_j^\alpha \quad \text{with} \quad \alpha \in \{x, y, z\}. \quad (33)$$

The u_{ij} are antisymmetric Hermitian link operators with eigenvalues ± 1

$$u_{ij} = -u_{ji}, \quad u_{ij}^2 = 1, \quad u_{ij}^\dagger = u_{ij} \quad (34)$$

The link operators commute with the Hamiltonian, $[H, u_{ij}] = 0$, so they are local symmetries. In this form, the Hamiltonian is representing a tight binding model of free Majorana fermions hopping along the lattice, with tunneling

couplings that depend on the eigenvalues of link operators which can be thought of as a classical \mathbb{Z}_2 gauge field. One can assign a configuration $\{u\}$ to all link operators and diagonalize the resulting quadratic Hamiltonian in Majorana operators directly and obtain the spectrum and groundstate energy for $H\{u\}$. But which configuration $\{u\}$ corresponds to the global minimum of the energy? This question has been answered by Lieb (1994) [15]. The groundstate lies in the sector with $B_p = 1 \ \forall p$ and since the B_p operators are the only gauge invariant objects, every gauge fixing choice $\{u\}$ which leads to this particular configuration for B_p is equivalent. Therefore, our goal is to find a configuration $\{u\}$ which leads to $B_p = 1 \ \forall p$.

Next, we define the vortex operator W_p as

$$W_p = \prod_{(i,j) \in \partial P} u_{ij} \quad \text{where} \quad \begin{cases} i \in & \text{even sublattice} \\ j \in & \text{odd sublattice} \end{cases} . \quad (35)$$

The vortex operator can be simplified as below

$$\begin{aligned} W_p &= u_{12}^x u_{32}^y u_{34}^z u_{54}^x u_{56}^y u_{16}^z \\ &= -(i)^6 c_1^x c_2^x c_2^y c_3^y c_3^z c_4^z c_4^x c_5^x c_5^y c_6^y c_6^z c_1^z \\ &= \sigma_1^y D_1 \sigma_2^z D_2 \sigma_3^x D_3 \sigma_4^y D_4 \sigma_5^z D_5 \sigma_6^x D_6 , \end{aligned} \quad (36)$$

where we used $ic_j^x c_j^y = -\sigma_j^z D_j$ and cyclic permutations. Considering the fact that $[W_p, H] = [W_p, D_i] = 0$, in the physical subspace where $D_j = 1$ we recover $W_p = B_p$. Therefore, the uniform choice of $u_{ij} = 1$ for every link will lead us to the groundstate in the extended (not yet projected) space with $B_p = 1$. In order to find the physical groundstate, we apply the global projector \mathbf{D} to project out the unphysical states

$$|\psi_w\rangle_{\text{physical}} = \mathbf{D} |\psi_u\rangle_{\text{extended}} , \quad \text{where} \quad \mathbf{D} = \prod_{i=1}^N P_i \quad (37)$$

Now we are at a point to explain in detail why the operators \hat{O}_1 and \hat{O}_2 can create vortices in the system. As mentioned earlier, if we flip the sign of the eigenvalue of the vortex operator at p , a vortex will be created in the system. Looking back at Equ.35, we see that the vortex configuration $\{W_p\}$ is created by fixing the gauge at every link $\{u_{ij}\}$. Therefore, by changing the link operators, we can move between vortex sectors. Starting from a vortex-free sector with all link operators being $+1$, applying \hat{O}_1 on site a will leave the σ_a^z untouched while flipping the σ_a^x and σ_a^y . Consequently, this will change the sign of the eigenvalue of the u_{ij} for x-link and y-link attached to site a , leaving the system with $B_{p_1} = -1$ and $B_{p_2} = -1$. We can also move the vortices around in the system, by consecutively applying these operators on the particular sites in a path for which we want to move the vortices along. As an example, the red path shown in the Fig.6 corresponds to the operator

$$\hat{O} = \exp(-i\frac{\pi}{2}\sigma_i^z) \exp(-i\frac{\pi}{2}\sigma_j^x) \quad (38)$$

In general, we can define string operators to move the vortices anywhere in the system along the string, similar to the example above. To create such a string operator is straightforward now. If the string passes through a link, we need to apply an operator on one of the sites connected to that α -link which carries σ^α in the exponent. Before continuing, we need to make a convention. A sharp reader might point out that applying the operator $\hat{O}' = \exp(-i\frac{\pi}{2}\sigma_l^z) \exp(-i\frac{\pi}{2}\sigma_k^x)$ instead of \hat{O} creates the same pair of vortices in the system. For consistency reasons, we therefore use the convention that if a string is passing through a link, the corresponding string operator is built up by picking the even site on the link. Having said all of this, a generic string operator is defined as

$$\hat{S} = \prod_{\alpha\text{-links}} \exp(-i\frac{\pi}{2}\hat{\sigma}_\alpha^\alpha) . \quad (39)$$

This string operator will create two vortices at the ending points of the string which passes through the α -links. The manipulation of link operators using these string operators is practically equivalent to changing the sign of the couplings

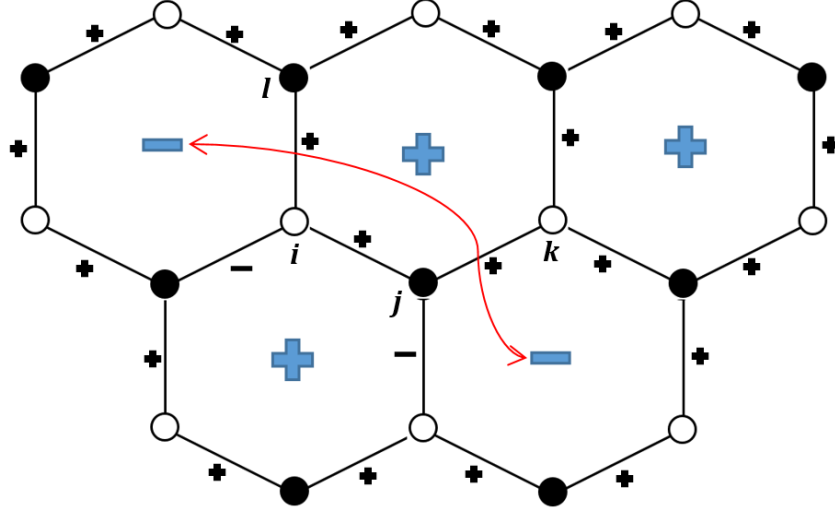


Figure 6: Two vortices connected by a string operator passing through several links. The white dots denote even lattice sites while the black dots are odd ones. By convention, the string operator is built up from operators acting on even sites.

J_{ij} corresponding to the link u_{ij} in the definition of the A_{ij} (see Equ.33). Therefore, in the RBM language one can simply redefine the Hamiltonian with the desired signs of J_{ij} for a particular vortex sector and then try to find the RBM representation for this new Hamiltonian through the approach explained in Section3. The only practical disadvantage of this vortex realization approach is that it is computationally expensive as the RBM should be trained again from scratch to find the representation for the excited state. An ideal approach is one where, given the representation for the groundstate, we would be able to directly and without further optimization steps find the representation for the excited state.

In principle, it is possible to directly manipulate the weight and bias parameters of the RBM, $\Omega = (a_k, b_{k'}, W_{kk'})$ to realize the vortices and find the excited state representation. Looking at Equ.22, we notice that there is a symmetry between the eigenvalues of physical spins and the value of parameters of the RBM. In other words, flipping a particular spin in site k is equivalent to flipping the sign of the RBM parameter sitting next to the σ_k^α in Equ.22 and/or adding a phase to it. In general, for a string operator $\hat{S}_a = \exp(-i\frac{\pi}{2}\hat{\sigma}_a^\alpha)$ we have:

$$\begin{aligned} \hat{S} |\Phi\rangle &= (-i\hat{\sigma}_a^\alpha) \sum_{\Xi} \Phi_M(\Xi; \Omega) |\Xi\rangle \\ &= \sum_{\Xi} e^{[(-1)^{\delta(\alpha-z)-1} a_a - i\frac{\pi}{2} \sigma_a^z] \sigma_a^z + \sum_{k \neq a} a_k \sigma_k^z} \times \\ &\quad \prod_{k'} \cosh \left((-1)^{\delta(\alpha-z)-1} W_{ak'} \sigma_a^z + \sum_{k \neq a} W_{kk'} \sigma_k^z + b_{k'} \right) \hat{\sigma}_a^\alpha |\Xi\rangle \end{aligned} \quad (40)$$

Therefore, applying \hat{S}_a on the RBM state, is equivalent to multiplying the bias parameter a_a and weight parameters $W_{ak'} \forall k'$ by $(-1)^{\delta(\alpha-z)-1}$ and then manually adding a $(-i\frac{\pi}{2}\sigma_a^z)$ phase angle to a_a , where $\sigma_a^z \in \{-1, +1\}$ is the eigenvalue of the z component of the spin on site a . The presence of the $(-1)^{\delta(\alpha-z)-1}$ factor is to ensure that when $\alpha = x$ or y , the $\hat{\sigma}_a^z$ eigenvalue is multiplied by a minus sign.

Need to fix the formula (40)

5 Results and Discussion

5.1 Groundstate

In this section, we present the results for the groundstate energy estimate of different system sizes for the proposed mapping discussed in Section3. These results are also compared to the exact analytical expression given in Equ.20. The

absolute value of the energies is plotted in Fig.7. All results for this and the following sections are for the *non-Abelian* phase $J_x = J_y = J_z = 1$.

The RBM has a simple fully-connected and two-layered architecture with an optimization value $\alpha = \frac{num_h}{num_v} = 2$ which is the ratio of the number of hidden nodes to the number of visible nodes. For lower values of α , the network does not give an accurate estimate of energies, while the larger values cause over-fitting and again lead to inaccurate results. For training, the configuration space of the network has been sampled for hundreds of times, depending on the lattice size, using the Metropolis algorithm. Moreover, the stochastic gradient descent algorithm has been used for optimization using a suitable number of iterations such that the network converges to a low enough minimum of the energy landscape.

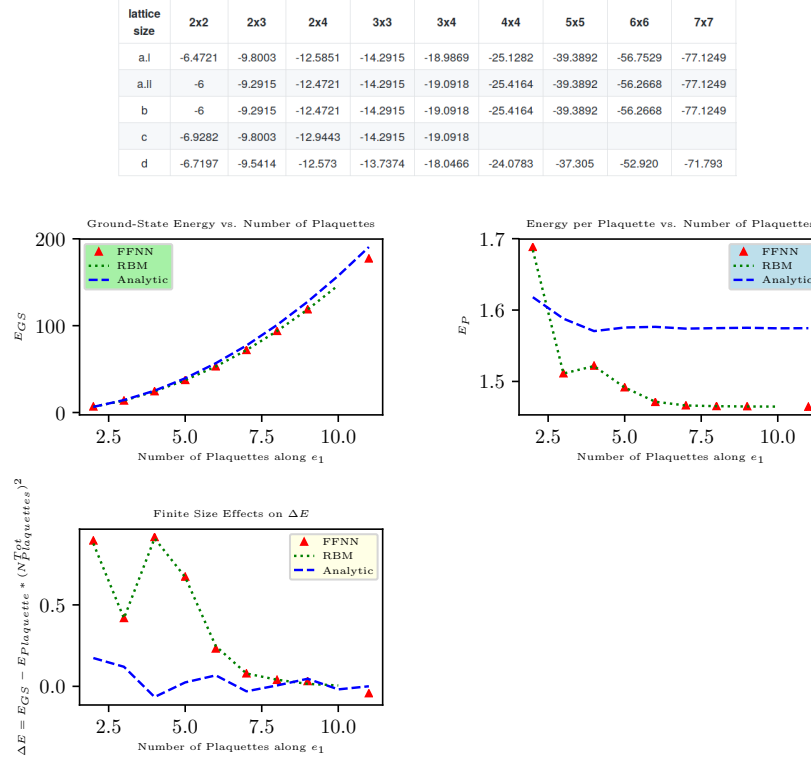


Figure 7: Numerical results for groundstate energy calculation using Restricted Boltzmann Machines (RBM) and Feed-Forward Neural Networks (FFNN) compared to the analytically obtained groundstate energy using Equ.19.

The numerical results obtained are shown in Fig.7. The different methods for computing the groundstate energy listed in the table are as follows:

- a) Analytic formula Equ.20 using
 - i. anti-periodic boundary conditions
 - ii. periodic boundary conditions
- b) The method of Kitaev and Pachos [2] [16]
- c) Create the Hamiltonian in NetKet and perform direct diagonalization
- d) RMB ($\alpha = 2$, train by $1k \times 10k$).

Based on the results obtained for the energy of the groundstate of the system, training of the network was tested and optimized by changing the learning rate for different training phases and iteration numbers. However, the outcome did not considerably change or improve and it seems that the above results are the most accurate results one can get for this particular network architecture.

In order to check the effect of the relative number of hidden and visible nodes on the outcome of the network, different values for α were tested, keeping other parameters fixed. The α parameter was changed just by changing the number of hidden nodes for a fixed system size (and hence fixed visible layer size) and the results are outlined in the table below, including the number of free parameters of the network and the time needed for the network to be trained. In order to

keep things simple, we focus on one particular spin system. All following results are based on the 5×5 lattice with exact analytic energy for the selected spin system is -39.3892 .

alpha	num_nh	num_para	energy	time(s)	notes
0.1	5	305	-27.7808(59)	171.6	
0.3	15	815	-33.4312(37)	455.0	
0.5	25	1325	-36.6024(22)	711.9	
1.0	50	2600	-37.2464(13)	1549	
1.5	75	3875	-37.1235(15)	2764	
2.0	100	5150	-37.3054(14)	5611	
3.0	150	7700	-37.3037(14)	8415	
4.0	200	10250	-37.1007(16)	11204	
6.0	300	15350	-37.2989(14)	18167	
8.0	400	20450	-37.1710(15)	26000	
10.0	500	25550	-37.1946(15)	32056	

Figure 8: Numerical results for the number of hidden nodes and its influence on energy calculations. $\alpha = \frac{num_h}{num_v}$.

From these results we can infer the following:

1. $\alpha = 2$ is the most suitable value for alpha. If it is too low, the fitting performance is not good; if too high, it will lead to over-fitting.
2. The training time is approximately proportional to the number of parameters. For each additional parameter, the training time is increased by about 1 second.
3. The result of the RBM is still far away from the analytic result.

The performance of FFNN

Below is the result of a FFNN with one layer. As the structure of the FFNN is similar to that of a no-visible-bias RBM(referred as novb RBM below), the performance of the one-layer FFNN is compared to that of no-visible-bias RBM.

alpha	num_nh	num_para	ffnn_energy	novb_rbm_energy	ffnn_time(s)	novb_rbm_time	notes
1.0	50	2550	-37.2401(15)	-37.1532(15)	2783	2754	
2.0	100	5100	-37.2958(14)	-36.8954(18)	4591	5476	
3.0	150	7650	-37.3007(14)	-37.2191(15)	6889	8331	

Figure 9: FFNN analysis.

The conclusion we reach is:

1. The FFNN trains faster than the RBM and performs better than the RBM with no bias.
2. But the FFNN's result again deviates by a similar margin from the analytic result.

One explanation for the slight deviation of the RBM result from the exact analytic result is that the RBM result is not in an exact eigenstate of the plaquette operators W_p . In fact, we find that all plaquette operator expectation values are close to zero, whereas the true ground state should have $W_p = +1$ for all plaquettes p . Thus the state we are finding seems to be a highly entangled state composed of the true ground state as well as certain excited states with small

energy. This seems to be a side effect of the gradient descent algorithm for minimizing the energy expectation value. We will have more to say about how to circumvent this constraint in Section 5.3.

5.2 Creating Vortex pairs and measuring their energy

As described in Section 4, there are three theoretically equivalent methods to create vortices:

- (a) modifying parameters of RBM
- (b) creating an auxiliary Hamiltonian and train again
- (c) transforming into auxiliary fermion representation and fixing u_{ij} s [2, 16]

We applied all three methods to a 3×3 lattice and computed the corresponding energy levels for excited states. The numeric result for the groundstate energy of a 3×3 lattice is $-13.7166(2)$, the theoretical gs energy is -14.2915 . For excited states obtained by flipping spins, the results we obtain are shown in the table below.

spins be flipped	energy of a	energy of b	energy of c
8xz	-11.7335(5)	-12.1070(51)	-13.9146
9xz	-11.7474(5)	-11.8873(57)	-13.9146
8y	unrealizable	-12.7447(37)	-13.9146

Figure 10: Energy of excited states with a pair of vortices in a 3×3 lattice system, measured through different methods as explained in the text.

We find that method a is more stable than method b. Both methods, a and b, deviate by a margin from the analytic result, namely method c. This can be again explained by the fact that the state from which these states are obtained by flipping, is not a true ground state but an entangled state. This can be confirmed by measuring the plaquette operators in the excited states we created and the result is again a value close to zero rather than $+1$ or -1 .

5.3 Quantum State Tomography for Groundstate

In this section we apply the technique discussed in Section 3.2 to reconstruct the wave function from measurements. In order to generate measurements, we first sample from an exact ground state by random measurements. To this end, we focus on the 2×2 lattice in order to keep training data and time short and solve for its ground state using exact diagonalization. We then sample this state using random measurement method. The last step is to train the RBM using the data obtained. The result is shown in Figure 11.

There are many intricate parameters which one can adjust during training, such as **learning rate, train-batch-num, sample-num, num-train-data**. Only with a suitable choice of parameters can one achieve a satisfactory result. For the example depicted, the size of the training data set is $8 \times 32 \times 2000$ and the variable α is 2. This choice leads to an overlap of 97 percent between the exact wave function and the learned one. On the other hand, the overlap can only reach 50 percent for a 2×2 lattice if the number of training data points is reduced to 2000. Moreover, we observe that, only in cases where the variables train-batch-num and sample-num both reach certain thresholds, the tomography can be successful. Otherwise, the overlap of the two wave functions will fluctuate around a very low level indefinitely. For the 2×2 lattice this threshold is reached when train-batch-num = sample-num = 1000 and higher.

explain

Plaquette Operator expectation values and spin flipping

Starting from the state obtained from tomography as discussed above, one can then realize spin flipping by modifying parameters of the RBM as described in Section 4. In order to verify that spin flipping takes us to the right excited state, we proceed by measuring the relevant plaquette operators each time. The results are as shown below.

For an RBM obtained by training from a ground state by tomography, the expectation values of its four plaquette operators are shown in Table 12. Flipping **spin number 5** along **yz-direction** will affect plaquettes **B** and **D**. The corresponding expectation value are shown in Table 13. Proceeding by flipping the spin of site 7, will affect the expectation values for plaquettes **A** and **D**, as shown in Table 14. Finally, by flipping the spin at the 3rd site, which affects plaquettes **A** and **B**, we close the circle and arrive back to the initial state, see Table 15.

explain: how is this a direction?

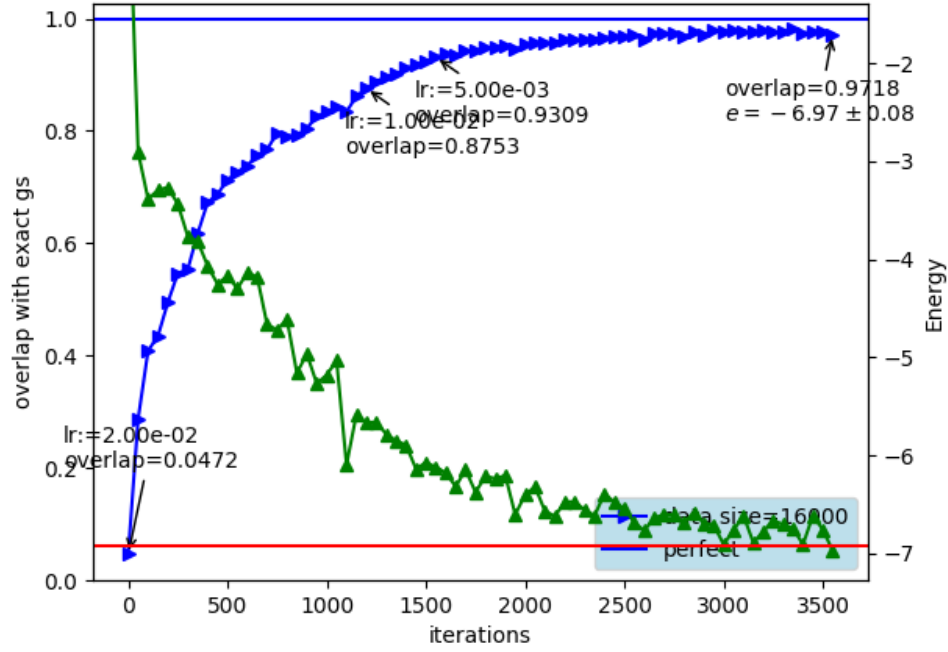


Figure 11: Energy and overlap results for QST of 2x2 lattice system.

A: 0.85984304
 B: 0.86507473
 C: 0.85363150
 D: 0.85877449

Figure 12: Expectation values of plaquette operators obtained by ground state tomography.

A: 0.85984304
 B: -0.86507473
 C: 0.85363150
 D: -0.85877449

Figure 13: Expectation values of plaquette operators obtained by flipping the spin at lattice point 5.

A: -0.85984304
 B: -0.86507473
 C: 0.85363150
 D: 0.85877449

Figure 14: Expectation values of plaquette operators obtained by flipping the spin at lattice point 7.

6 Conclusion

It is worth to evaluate the energy of vortices by method c for large systems in the future.

A: 0.85984304
 B: 0.86507473
 C: 0.85363150
 D: 0.85877449

Figure 15: Expectation values of plaquette operators obtained by flipping the spin at lattice point 3.

7 Acknowledgement

YMSC, Martin Duy Tat,

References

- [1] A. Kitaev, *Anyons in an exactly solved model and beyond*, *Annals of Physics* **321** (2006) 2â€š111.
- [2] A. Kitaev, *Fault-tolerant quantum computation by anyons*, *Annals of Physics* **303** (2003) 2â€š30.
- [3] G. Jackeli and G. Khaliullin, *Mott insulators in the strong spin-orbit coupling limit: From heisenberg to a quantum compass and kitaev models*, *Physical Review Letters* **102** (2009) .
- [4] K. S. Tikhonov, M. V. Feigelâ€šman and A. Y. Kitaev, *Power-law spin correlations in a perturbed spin model on a honeycomb lattice*, *Physical Review Letters* **106** (2011) .
- [5] D.-L. Deng, X. Li and S. Das Sarma, *Machine learning topological states*, *Physical Review B* **96** (2017) .
- [6] G. Carleo, K. Choo, D. Hofmann, J. E. T. Smith, T. Westerhout, F. Alet et al., *Netket: A machine learning toolkit for many-body quantum systems*, *SoftwareX* (2019) 100311.
- [7] G. Torlai, G. Mazzola, J. Carrasquilla, M. Troyer, R. Melko and G. Carleo, *Neural-network quantum state tomography*, *Nature Physics* **14** (2018) 447â€š450.
- [8] P. Jordan and E. P. Wigner, *About the Pauli exclusion principle*, *Z. Phys.* **47** (1928) 631.
- [9] H.-D. Chen and Z. Nussinov, *Exact results of the kitaev model on a hexagonal lattice: spin states, string and brane correlators, and anyonic excitations*, *Journal of Physics A: Mathematical and Theoretical* **41** (2008) 075001.
- [10] P. Schmoll and R. Orâ€šzs, *Kitaev honeycomb tensor networks: Exact unitary circuits and applications*, *Physical Review B* **95** (2017) .
- [11] E. H. Lieb, *Flux phase of the half-filled band*, *Physical Review Letters* **73** (1994) 2158â€š2161.
- [12] N. Le Roux and Y. Bengio, *Representational power of restricted boltzmann machines and deep belief networks*, *Neural Computation* **20** (2008) 1631 [<https://doi.org/10.1162/neco.2008.04-07-510>].
- [13] C. Nayak, S. H. Simon, A. Stern, M. Freedman and S. Das Sarma, *Non-abelian anyons and topological quantum computation*, *Reviews of Modern Physics* **80** (2008) 1083â€š1159.
- [14] A. J. Leggett, *Lecture 26, the kitaev models*, **PHYS598PTD**, University of Illinois, Department of Physics (2013) .
- [15] G. Kour and R. Saabne, *Real-time segmentation of on-line handwritten arabic script*, in *Frontiers in Handwriting Recognition (ICFHR), 2014 14th International Conference on*, pp. 417â€š422, IEEE, 2014.
- [16] J. K. Pachos, *Introduction to Topological Quantum Computation*. Cambridge University Press, USA, 1st ed., 2012.